**Please cite the Published Version**

**Additional Information:** This is an Author Accepted Manuscript of an article published in Langmuir, by the American Chemical Society.

1 **Principal Component Analysis to Determine the Surface Properties that Influence the**

2 **Self-Cleaning Action of Hydrophobic Plant Leaves**

3

4

5

6 Fabien Saubade[a], Lisa I. Pilkington[b], Christopher M. Liauw[a], Luciana C. Gomes[c], Jake

7 McClements[d], Marloes Peeters[d], Mohamed El Mohtadi[e] Filipe Mergulhão[c] and Kathryn A.

8 Whitehead[a]*

9

10

11 [a] Microbiology at Interfaces, Department of Life Sciences, Manchester Metropolitan

12 University, Manchester, UK.

13 [b] School of Chemical Sciences, University of Auckland, Auckland 1010, New Zealand

14 [c] LEPABE— Laboratory for Process Engineering, Environment, Biotechnology and Energy,

15 Faculty of Engineering, University of Porto, Rua Dr.Roberto Frias, 4200-465 Porto, Portugal

16 [d] School of Engineering, Newcastle University, Merz Court, Claremont Road, Newcastle

17 Upon Tyne NE1 7RU, UK

18 [e] Department of Biology, Edge Hill University, Ormskirk, Lancashire, L39 4QP, UK

19

20 *Corresponding Author: K. A. Whitehead, Manchester Metropolitan University, UK.

21 E-mail address K.A.Whitehead@mmu.ac.uk

22

23    **ABSTRACT**

24    It is well established that many leaf surfaces display self-cleaning properties. However, an

25    understanding of how the surface properties interact is still confounding. Consequently, twelve

26    different leaf types were selected for analysis due to their water repellency and self-cleaning

27    properties. The most hydrophobic surfaces demonstrated splitting of the $v_s$ $CH_2$ and $v$ $CH_2$

28    bands, ordered platelet-like structures, crystalline waxes, high surface roughness values, high

29    total surface free energy and apolar components of surface energy, and low polar and Lewis

30    base components of surface energy. The surfaces that exhibited the least roughness and high

31    polar and Lewis base components of surface energy had intracuticular waxes, yet still

32    demonstrated self-cleaning action. Principal component analysis demonstrated that the most

33    hydrophobic species shared common surface chemistry traits with low intra-class variability,

34    whilst the less hydrophobic leaves had highly-variable surface chemistry characteristics.

35    Despite this, we have shown through partial least squares regression that leaf water contact

36    angle (i.e. hydrophobicity) can be predicted using attenuated total reflectance Fourier transform

37    infrared spectroscopy surface chemistry data with excellent ability. This is the first time that

38    such a statistical analysis has been performed on a complex biological system. This model

39    could be utilised to investigate and predict the water contact angles of a range of biological

40    surfaces. An understanding of the interplay of properties is extremely important when

41    producing optimised biomimetic surfaces.

42

43    **Keywords:** Biomimetic; plant; roughness; superhydrophobic; wax; self-cleaning.

44

**INTRODUCTION**

There has been significant interest directed towards producing biomimetic surfaces with controlled surface wetting properties.[1] Much of this work has concentrated on altering surface topography and chemistry to produce superhydrophobic surfaces. It is generally considered that the topography of plant surfaces is the main factor influencing water contact angle (WCA), and hence water repellency.[2,3] Specifically, hierarchical structures at the macro and micro levels (the Lotus effect) are associated with superhydrophobicity of leaf surfaces.[4] The leaves are also self-cleaning, meaning that rolling droplets can remove microorganisms and other contaminants from their surfaces. Numerous biomimetic surfaces have been developed which emulate the topography of superhydrophobic leaves to achieve self-cleaning, water repellency, and anticontamination properties.[5–8] However, many self-cleaning surfaces produced with biomimetic topographies still require chemical modification to exhibit superhydrophobicity. Many plant surfaces are hydrophobic (WCA >110°) or superhydrophobic (WCA > 150°).[9] However, in nature, there are also several leaf surfaces that display self-cleaning and water-repellent behaviours, and yet they are not superhydrophobic and may not have predominant topographical features.

It is well established that the wax layer on leaf surfaces, in particular epicuticular wax crystals, makes an essential contribution to surface hydrophobicity.[10] The chemical compositions of such waxes from numerous leaf surfaces have been determined.[11–17] However, the exact relationship between surface chemistry and topography, in addition to their influence on surface physiochemistry is not fully understood. Consequently, producing biomimetic surfaces that maintain their anti-wetting features still presents a significant challenge. Thus, an understanding of the key surface properties that result in the water repellency of natural surfaces is essential to further the development of biomimetic surfaces.

The aim of this work was to determine the relationship between the surface topography, chemistry, and physiochemistry of a selection of plant leaves that demonstrated self-cleaning properties. This was implemented through a combination of complementary experimental techniques and modelling methods to identify the key parameters that resulted in the self-cleaning properties of these natural surfaces. This information is vitally important to many aspects of industry where producing low-cost and consistent biomimetic surfaces is a priority.

**EXPERIMENTAL**

*Leaf collection*

Plant leaves were selected based on their ability to repel water. Many leaf types were sprayed with water for 1 min and then immediately assessed. Those that exhibited no residual water droplets or spherical spray droplets on their surfaces were deemed the most hydrophobic, and therefore selected. Leaves from the following plants were collected (Westhoughton, Greater Manchester, UK) between the months of September and November 2017: *Aquilegia vulgaris* (Aquilegia), *Citrus sinensis* (Orange), *Gladiolus hybridus* (Gladioli), *Hosta sieboldiama* (Hosta), *Hyacinthus litwinovii* (Hyacinth), *Ilex aquifolium* (Holly), *Lathyrus odoratus* (Sweet pea), *Lupinus polyphyllus* (Lupin), *Nymphaea odorata* (Water lily), *Pelargonium graveolens* (Geranium), *Prunus laurocerasus* (Laurel), and *Rhododendron azaleastrum* (Azalea). Leaf samples were either used within 2-4 h of harvesting or stored at 4 °C for a maximum of 24 h before use. The leaves were stored individually in plastic bags until use to ensure that the loss of humidity from the leaf was reduced. A number of separate batches of mature leaves were collected on different days over the two-month experimental period ($n = 10$).

*Determination of surface energy components*

4

94   The total surface free energy ($\gamma_s$) and the apolar ($\gamma_s^{LW}$), polar ($\gamma_s^{AB}$), Lewis acid ($\gamma_s^+$),

95 and Lewis base ($\gamma_s^-$) free energy components of the adaxial surfaces of the leaves were

96 determined using contact angle goniometry. The surface energy components of the leaves were

97 calculated according to the work by van Oss and colleagues.[18-20] A KRÜSS sessile drop

98 goniometer (GH11 KRÜSS, France) was used to perform the measurements with three test

99 liquids: HPLC grade water (BDH, UK), formamide (Sigma-Aldrich, UK), and diiodomethane

100 (Alfa Aesar, UK). For each plant species, except the *Rhododendron azaleastrum*, samples were

101 cut from different parts of the same leaf and attached to microscope slides using double-sided

102 adhesive tape (3M, UK). In the case of *Rhododendron azaleastrum*, individual leaves were

103 used for each test liquid. For all test liquids, the droplet volume was 5 µL and was dispensed

104 using a micro-syringe dedicated to a single solvent.

105   For each plant species, the van Oss and Good equations were used to obtain the surface

106 energy components from the contact angles of the three test liquids on the leaf surfaces.[18–20]

107 The surface free energy components of these three liquids were taken from Bos et al.[21]

108 (Supporting Information: Table S1).

109   The contact angles of each test liquid were obtained from five different areas on the

110 leaf, therefore average values were used to obtain the physicochemical parameters. The

111 statistical error in the calculated surface energy components was estimated from the contact

112 angles of each test liquid by using propagation of error principles. The interfacial free energy

113 ($\Delta G_{iwi}$) was used as a measure of the hydrophobicity of a leaf surface where greater (negative)

114 $\Delta G_{iwi}$ values related to more hydrophobic surfaces.

115

116 *Optical profilometry and scanning electron microscopy (SEM)*

117   The surface topographies of the leaves were investigated using a previously described

118 method with a MicroXAM (phase shift) surface mapping microscope (ADE corporation, XYZ

119     model 4400 ml system, USA).[22] The optical profilometer used an AD phase shift controller

120     (Omniscan, UK). A MAPVIEW AE 2.17 (Omniscan, UK) image analysis system was utilised

121     to obtain the average surface roughness ($S_a$), root mean square roughness ($S_q$), and average

122     peak-to-valley roughness ($S_{pv}$) (n=10).

123             SEM images were obtained using a Supra 40VP SEM (Carl Zeiss Ltd., UK) with an

124     adapted protocol.[23] The leaf samples were soaked for 24 h at 4 °C in 4 % v/v glutaraldehyde

125     (Agar Scientific, UK). The leaf samples were removed and the excess glutaraldehyde was

126     washed from the leaf surface using sterile water. The leaf samples were then dried overnight.

127     Following drying, the samples were cut into ca. 6 mm$^2$ coupons. The adaxial sides of the leaves

128     were fixed to carbon pads on SEM stubs (Agar Scientific, UK). The fixed leaf surfaces were

129     sputter coated with gold (Polaron, UK) using the parameters: 5 mA, < 0.1 mbar, and 800 V in

130     argon gas.

131

132     *Attenuated total reflectance Fourier transform infrared spectroscopy (ATR-FTIR)*

133             ATR-FTIR analysis was performed on leaf samples using a Spectrum Two FT-IR

134     Spectrometer (PerkinElmer, UK) fitted with a UATR single bounce ATR accessory with a

135     diamond (refractive index 2.40) internal reflection element (IRE) (45° angle of incidence) and

136     LiTaO$_3$ detector. For each leaf sample, five different areas were analysed obtaining the spectra

137     over the range of 450 to 4000 cm$^{-1}$. Spectra were made up of four scans with the resolution set

138     to 4 cm$^{-1}$ and the results were expressed in absorbance. It is worth noting that the penetration

139     depth of the evanescent wave into the leaf surface from the IRE can be estimated to be 1.5 μm

140     at 2900 cm$^{-1}$ and 6.1 μm at 700 cm$^{-1}$. Calculations based on the equation by F. Mirabella

141     assumed the leaf surface to be mainly hydrocarbon, i.e. paraffin wax (refractive index 1.45).[24]

142     Due to the topographical aspects potentially affecting contact with the IRE, the spectra were

143     not corrected for wavelength dependent penetration depth.

144

*Statistical analysis*

146     Error bars were representative of the standard deviation or ± 5% error. One-way

analysis of variance (ANOVA) followed by Newman-Keuls tests were performed using R.

3.4.1 software. Differences between samples were considered statistically significant for *p*

values < 0.05.

150

*Principal component analysis (PCA)*

152     PCA was carried out on the ATR-FTIR data measured using R (version 3.2.2, R Core

Team, 2015)[25] and R Studio (version 0.99.486, R Studio Team).[26] PCA analysis was performed

using the prcomp function as part of the stats package by singular value decomposition of the

centred and scaled data matrix.[25] Results of this analysis were visualised using the factoextra

package (version 1.0.5) and ggplot2.[27]

157

*Partial least squares regression (PLSR)*

159     PLSR was carried out on the ATR-FTIR data using R (version 3.2.2, R Core Team,

2015)[25] and R Studio (version 0.99.486, R Studio Team, 2015).[26] PLSR analysis was performed

using the plsr function as part of the pls package (version 2.7-1).[28] The kernel algorithm was

used on a mean-centred predictor and response data matrix. Leave-one-out cross-validation

was utilised to optimise the number of components (8) to be used in the final model.

164

**RESULTS AND DISCUSION**

*Physicochemical properties of the leaf surfaces*

167     The physicochemical parameter values are represented in radar graphs (Figure 1) to

provide a physicochemical map for each leaf surface. Furthermore, the physicochemical

169    parameters of the twelve leaf surfaces are presented in Table 1. The $\gamma_s^{LW}$ values of all the leaves

170    were higher than their corresponding $\gamma_s^{AB}$ values. Therefore, all the leaves investigated had

171    non-polar adaxial surfaces. The three most hydrophobic leaves (*Gladiolus hybridus*, *Lupinus*

172    *polyphyllus*, and *Lathyrus odoratus*) demonstrated high $\gamma_s^{LW}$ values and substantially lower

173    $\gamma_s^{AB}$, $\gamma_s^+$, and $\gamma_s^-$ values. These patterns were represented in the graphs in Figure 1 by thin

174    asymmetric diamond shapes with the long arm pointing upwards. The base and short downward

175    arm of the diamond was formed from the relatively insignificant $\gamma_s^{AB}$, $\gamma_s^+$, and $\gamma_s^-$ contributions

176    to the total surface energy. The less hydrophobic surfaces had higher $\gamma_s^-$ values which led to

177    graphs with wider bases and various triangular shapes.

178
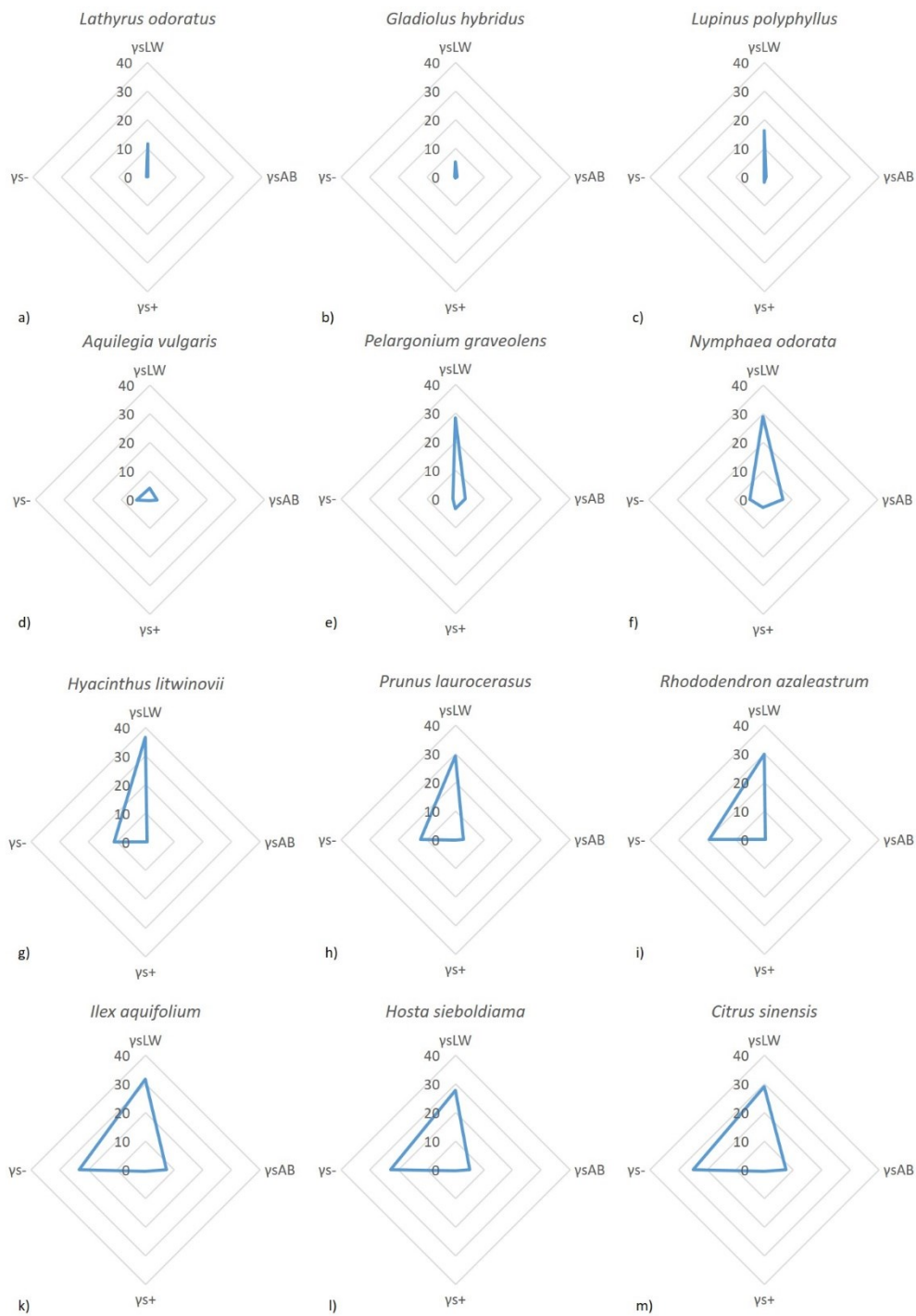
**Figure 1.** Radar graphs showing the magnitude of the surface energy components for each leaf type.

Table 1. Physicochemical parameters of the adaxial surface of the leaf samples. The values are expressed in mJ/m$^2$ and the errors are in parenthesis.

| Leaf | $\Delta G_{iwi}$ | | $\gamma_s$ | | $\gamma_s^{LW}$ | | $\gamma_s^{AB}$ | | $\gamma_s^{+}$ | | $\gamma_s^{-}$ | |
|---|---|---|---|---|---|---|---|---|---|---|---|---|
| *Lathyrus odoratus* | -91.7 | (9.4) | 11.6 | (1.0) | 11.6 | (0.9) | 0.1 | (0.3) | 0.0 | (0.0) | 0.38 | (0.43) |
| *Gladiolus hybridus* | -91.3 | (12.2) | 6.0 | (1.2) | 5.4 | (1.0) | 0.6 | (0.7) | 0.4 | (0.4) | 0.25 | (0.44) |
| *Lupinus polyphyllus* | -74.7 | (10.6) | 16.4 | (1.4) | 16.2 | (0.7) | 0.2 | (1.2) | 1.8 | (0.7) | 0.00 | (0.06) |
| *Aquilegia vulgaris* | -64.2 | (16.4) | 6.9 | (2.1) | 4.2 | (1.0) | 2.7 | (1.8) | 0.4 | (0.4) | 4.9 | (2.90) |
| *Pelargonium graveolens* | -54.0 | (7.9) | 31.5 | (1.5) | 28.1 | (0.9) | 3.4 | (1.2) | 3.3 | (0.7) | 0.9 | (0.57) |
| *Nymphaea odorata* | -41.1 | (6.5) | 35.9 | (1.3) | 29.0 | (0.9) | 6.9 | (1.0) | 2.6 | (0.5) | 4.5 | (1.01) |
| *Hyacinthus litwinovii* | -38.3 | (7.9) | 37.1 | (1.4) | 36.6 | (0.6) | 0.5 | (1.3) | 0.0 | (0.0) | 10.9 | (1.97) |
| *Prunus laurocerasus* | -30.1 | (6.8) | 32.0 | (1.2) | 29.1 | (0.6) | 2.8 | (1.1) | 0.2 | (0.1) | 12.2 | (1.91) |
| *Rhododendron azaleastrum* | -14.5 | (11.1) | 30.3 | (2.3) | 29.9 | (0.6) | 0.4 | (2.2) | 0.0 | (0.0) | 19.3 | (3.76) |
| *Ilex aquifolium* | -6.0 | (10.5) | 38.8 | (2.2) | 31.5 | (0.6) | 7.3 | (2.1) | 0.6 | (0.3) | 23.1 | (3.98) |
| *Hosta sieboldiama* | -5.7 | (32.6) | 32.6 | (2.8) | 27.6 | (1.2) | 5.0 | (2.6) | 0.3 | (0.3) | 22.8 | (3.50) |
| *Citrus sinensis* | -2.3 | (10.2) | 36.4 | (2.2) | 29.0 | (0.6) | 7.5 | (2.1) | 0.6 | (0.3) | 24.8 | (3.99) |

*Surface topography*

The topographies of the leaves were investigated at the macro, micro, and nanoscale scale to comprehensively analyse the morphology of the surface features. Low magnification SEM images (Figure 2) revealed that the macro topographies of the leaves were most commonly characterised by platelet-type features (Figure 2a, g, j, m, p, s, ee, and hh). However, some exhibited quite different surface topographies, including homogenous distributions of raised nodules (Figure 2d), subtle network structures (Figure 2v and y), and very flat, almost featureless surfaces (Figure 2bb). Optical profilometry images highlighted the micro topographies of the leaf surfaces and revealed more detailed information regarding the varied
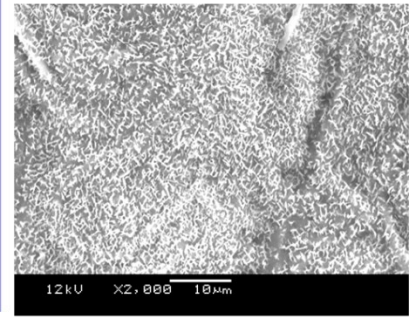
195    platelet-like morphology. For example, the average platelet feature length ranged from 10 to

196    45 µm and some were very regular in shape (Figure 2h, n, and ff), whilst others were far more

197    irregular (Figure 2b, k, t, and ii). The nano features of the surface topographies were

198    investigated using high magnification SEM. The images demonstrated that wax nanocrystals

199    were present on all the leaf surfaces in varying amounts. The most hydrophobic surfaces

200    (Figure 2c, 2f, 2i, and 2l) exhibited dense distributions of wax nanocrystals, whilst the less

201    hydrophobic surfaces had far smaller amounts (Figure 2x, aa, dd, gg, and jj).
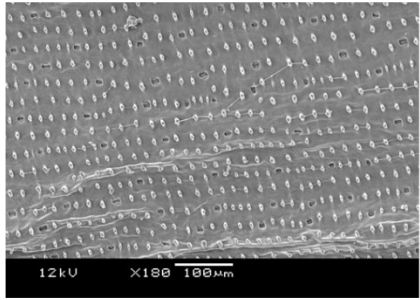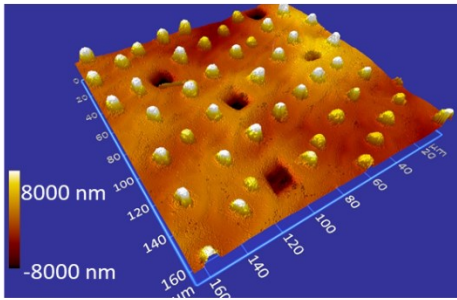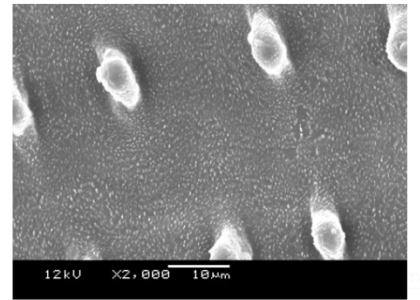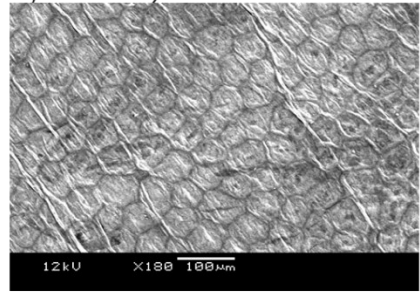
202
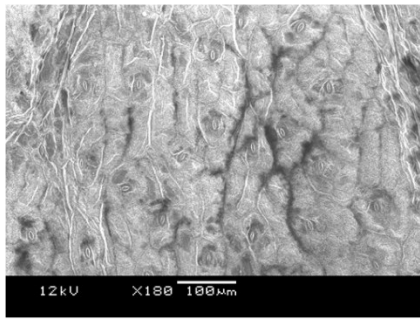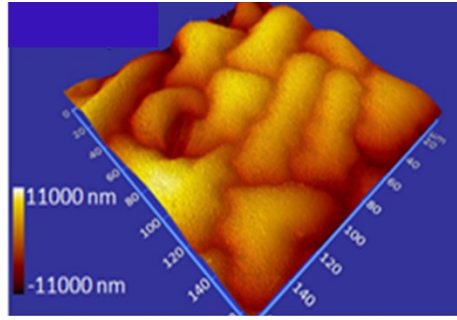
a) *Lathyrus odoratus*  b)  c)

d) *Gladiolus hybridus*  e)  f)

g) *Lupinus polyphyllus*  h)  i)
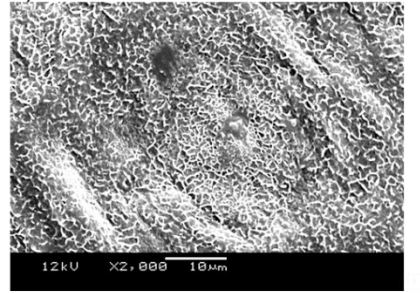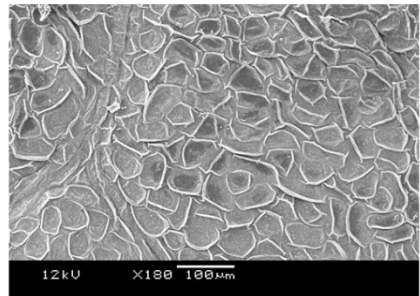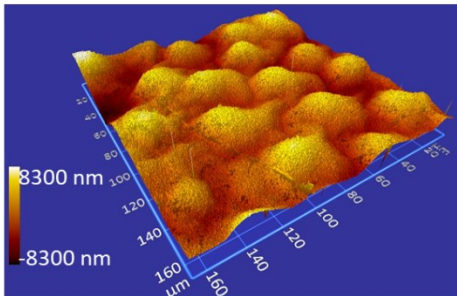
j) *Aquilegia vulgaris*  k)  l)
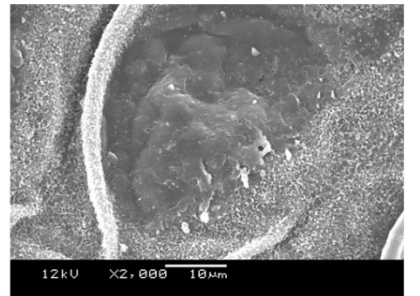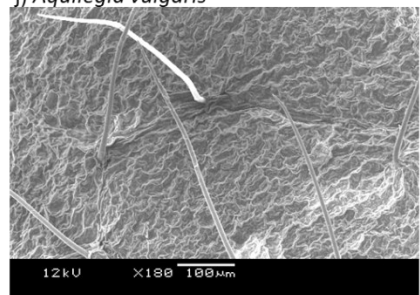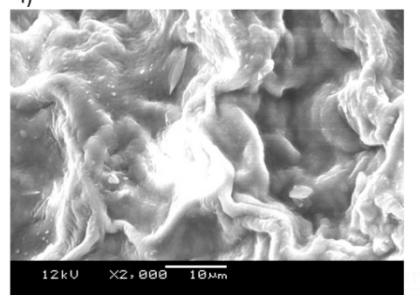
m) *Pelargonium graveolens*  n)  o)

p) *Nymphaea odorata*  q)  r)

203

s) *Hyacinthus litwinovii*
t)
u)

v) *Prunus laurocerasus*
w)
x)

y) *Rhododendron azaleastrum*
z)
aa)

bb) *Ilex aquifolium Ilex aquifolium*
cc)
dd)

ee) *Hosta sieboldiama*
ff)
gg)

hh) *Citrus sinensis*
ii)
jj)
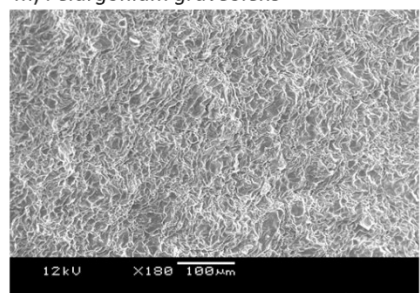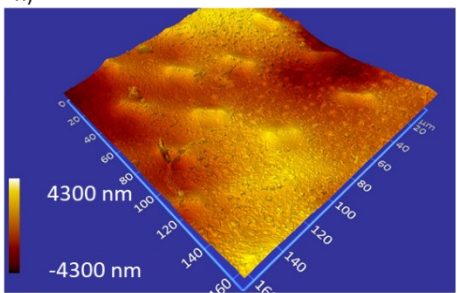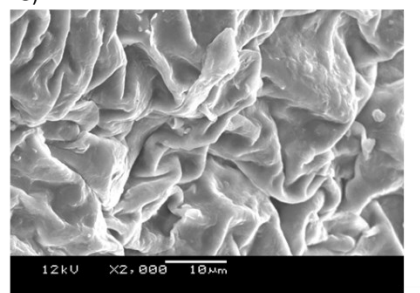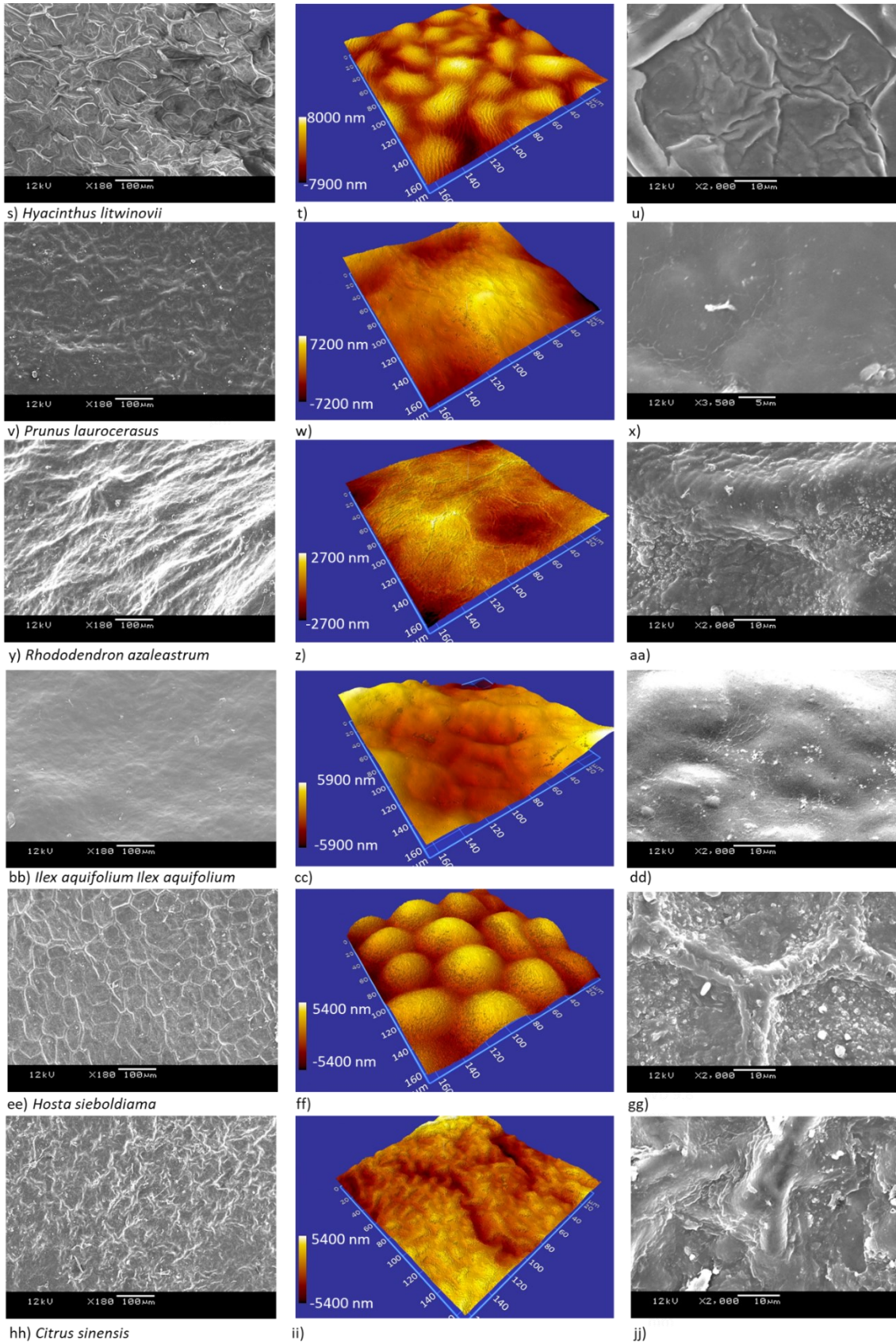
**Figure 2.** Optical profilometry and SEM images of the adaxial surfaces of the leaf samples demonstrating their macro, micro, and nano surface topographies.

207     Table 3 presents the surface roughness values for each leaf type. The results demonstrate that

208     the more hydrophobic surfaces generally had the greatest roughness values, whilst the least

209     hydrophobic surfaces had the lowest roughness values. However, there were some exceptions

210     to this trend. For example, the *Pelargonium graveolens* had the largest roughness values.

211     Similarly, the *Hyacinthus litwinovii* leaf, which was not one of the most hydrophobic surfaces,

212     also had large $S_a$ (2.8 μm) and $S_{pv}$ (118.9 μm) values. Generally, the least hydrophobic surfaces

213     had less defined surface features. The exception was the *Hosta sieboldiama*, which had low

214     surface roughness values but still demonstrated defined platelet-type features on its surface

215     (Figure 2n).

216

217     **Table 3.** Surface roughness parameters of the leaf samples obtained from the optical

218     profilometry data. The standard deviations are indicated in parenthesis.

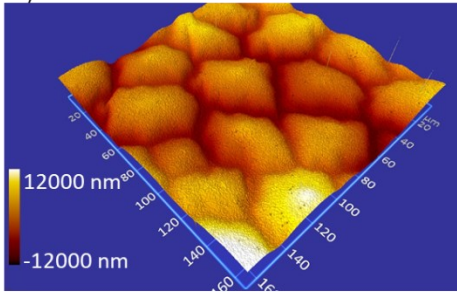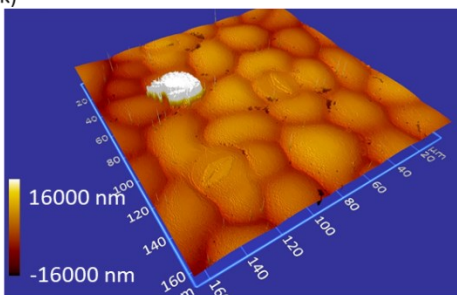| Leaf | $S_a$ (μm) | | $S_q$ (μm) | | $S_{pv}$ (μm) | |
|---|---|---|---|---|---|---|
| *Lathyrus odoratus* | 3.2 | (0.6) | 3.9 | (0.7) | 36.5 | (8.5) |
| *Gladiolus hybridus* | 2.6 | (0.9) | 3.6 | (1.1) | 69.2 | (20.1) |
| *Lupinus polyphyllus* | 4.3 | (1.4) | 5.3 | (1.8) | 41.1 | (10.1) |
| *Aquilegia vulgaris* | 2.9 | (0.4) | 3.6 | (0.6) | 41.5 | (8.1) |
| *Pelargonium graveolens* | 5.9 | (1.5) | 9.4 | (2.0) | 148.2 | (15.2) |
| *Nymphaea odorata* | 0.8 | (0.1) | 1.1 | (0.2) | 9.9 | (3.0) |
| *Hyacinthus litwinovii* | 2.8 | (0.9) | 3.5 | (1.2) | 118.9 | (19.2) |
| *Prunus laurocerasus* | 2.0 | (0.4) | 2.4 | (0.4) | 13.4 | (2.8) |
| *Rhododendron azaleastrum* | 2.2 | (1.1) | 2.9 | (1.5) | 40.0 | (21.4) |
| *Ilex aquifolium* | 1.2 | (0.2) | 1.4 | (0.2) | 9.0 | (2.0) |
| *Hosta sieboldiama* | 2.0 | (0.4) | 2.5 | (0.5) | 28.8 | (11.5) |
| *Citrus sinensis* | 1.6 | (0.4) | 2.1 | (0.5) | 31.9 | (18.6) |

*Surface chemistry*

220      ATR-FTIR was used to identify the major classes of chemical species within the first

221    few microns of the adaxial surfaces of the leaves (Figures 3 and 4). All the leaf spectra generally

222    featured a relatively strong and broad hydrogen-bonded OH stretching band centred at 3300

223    $cm^{-1}$ (Peak A, Figure 3). For the *Prunus laurocerasus* and *Hosta sieboldiama*, this band was

224    noticeably weak relative to the C-H stretching bands (centred at ca. 2900 $cm^{-1}$). However, for

225    the *Nymphaea odorata*, the OH band was more intense than the C-H band. The *Gladiolus*

226    *hybridus*, *Citrus sinensis*, *Hyacinthus litwinovii*, and *Pelargonium graveolens* leaves had an

227    OH band that was of near equal intensity to the C-H band. The OH band can be assigned to

228    alcohols, carboxylic acids, and water. All the leaves exhibited two bands at 2916 and 2846 $cm^{-1}$

229    (asymmetric ($\nu_{as}$ $CH_2$) and symmetric ($\nu_s$ $CH_2$) methylene C-H stretching, respectively),

230    which corresponded to the non-polar hydrocarbon compounds on their surfaces. The

231    accompanying methylene C-H deformation (scissoring ($\nu_s$ $CH_2$)) and C-H rocking ($\rho$ $CH_2$)

232    bands centred at ca. 1450 and 720 $cm^{-1}$, respectively, were also evident. All the leaves featured

233    carbonyl (C=O) bearing species that generally absorbed at 1735 $cm^{-1}$, indicating the possible

234    dominance of ester-based compounds present in the leaf composition. A broad collection of

235    bands centred at ca. 1630 $cm^{-1}$ was also evident on all the leaves which can be assigned mainly

236    to H-O bending modes of the water molecule. In all cases, except *Hosta sieboldiama* and to a

237    lesser extent *Prunus laurocerasus*, the absorbance of this band was indicative of the OH

238    stretching band. In the exceptional cases of *Hosta sieboldiama* and *Prunus laurocerasus*, there

239    was significant confounding with other chemical species that absorbed in the same region. For

240    *Hosta sieboldiama*, there was a strong and sharp band (1640 $cm^{-1}$) in this region. For all the

241    leaf surfaces, a band at 1055 $cm^{-1}$ was detected which could correspond to the C–O stretching

242    of primary alcohols that are present.
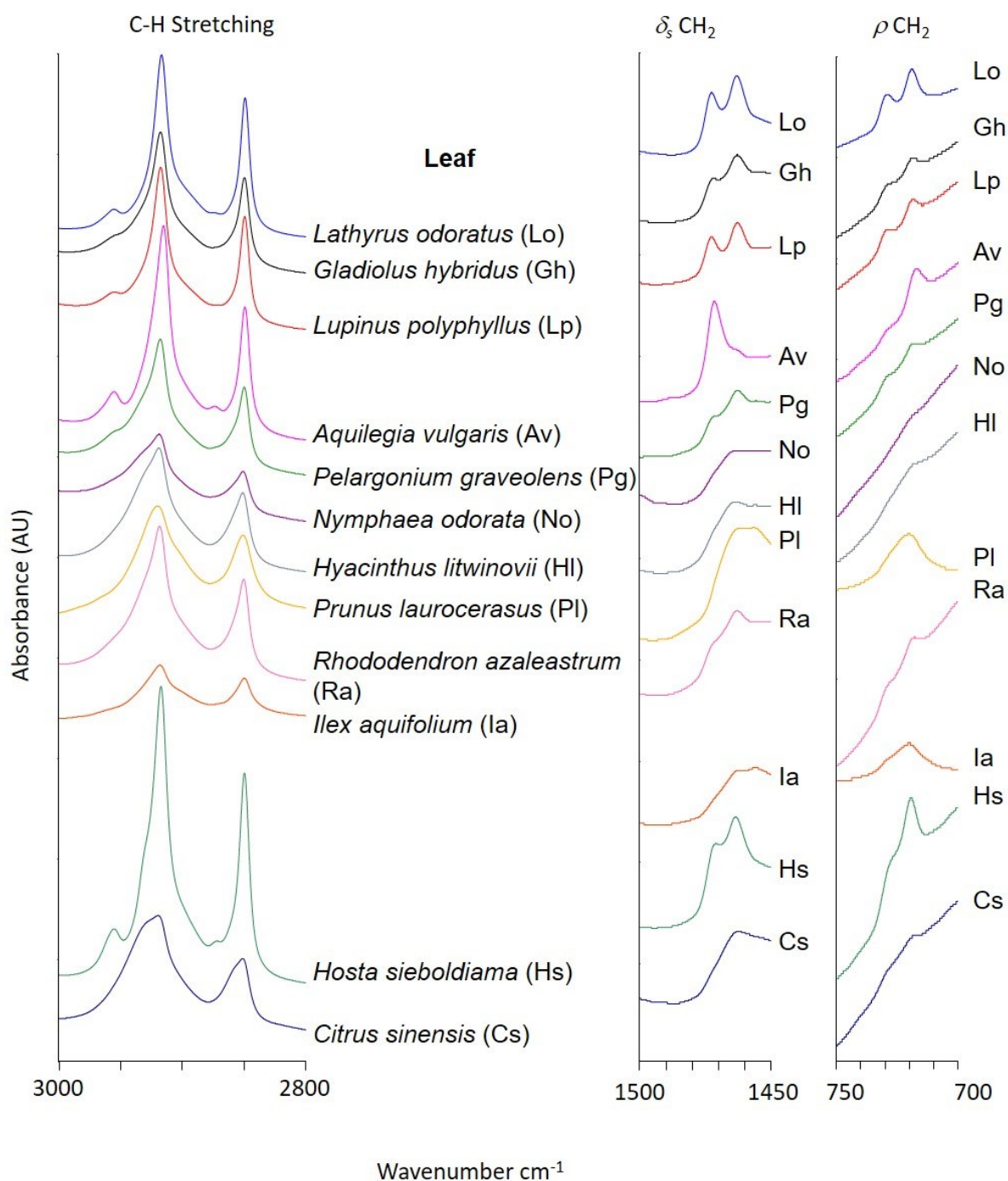
**Figure 3.** C-H stretching, C-H deformation, and C-H rocking regions of the ATR-FTIR spectra of the leaf samples showing variations in hydrocarbon content and structural ordering of wax components (splitting of the $\nu_s$ CH$_2$ and $\rho$ CH$_2$ bands). Lo: *Lathyrus odoratus*, Gh: *Gladiolus hybridus*, Lp: *Lupinus polyphyllus*, Av: *Aquilegia vulgaris*, Pg: *Pelargonium graveolens,* No: *Nymphaea odorata*, Hl: *Hyacinthus litwinovii*, Pl: *Prunus laurocerasus*, Ra: *Rhododendron azaleastrum*, Ia: *Ilex aquifolium*, Hs: *Hosta sieboldiama,* Cs: *Citrus sinensis*.

250    A band at 1032 cm$^{-1}$ was detected on the *Lathyrus odoratus*, *Nymphaea odorata*,

251    *Hyacinthus litwinovii*, *Prunus laurocerasus*, *Ilex aquifolium*, *Hosta sieboldiama*, and *Citrus*

252    *sinensis* leaf surfaces, which could correspond to the C–O stretching of secondary alcohols.

253    Interestingly, pronounced splitting of the $\nu_s$ CH$_2$ and $\rho$ CH$_2$ bands was detected in the spectra

254    of the *Gladiolus hybridus*, *Hosta sieboldiama*, *Lupinus polyphyllus*, and *Lathyrus odoratus*,

255    which can be assigned to the presence of highly crystalline wax structures (Figure 4). This was

256    also evident on the *Aquilegia vulgaris* and *Pelargonium graveolens* leaf surfaces but to a lesser

257    extent. The *Ilex aquifolium* and *Prunus laurocerasus* surfaces exhibited a single $\rho$ CH$_2$ band at

258    719 cm$^{-1}$, which could indicate a disordered (liquid-like) arrangement of long alkyl chains. The

259    *Hyacinthus litwinovii* and *Nymphaea odorata* showed weak $\nu_s$ CH$_2$ and $\rho$ CH$_2$ bands hindering

260    detection of splitting. The *Hosta sieboldiama* differed from the other surfaces in that it also

261    demonstrated a $\nu_{\alpha s}$ CH$_2$ band at 2925 cm$^{-1}$ and a C=O peak at 1640 cm$^{-1}$. Overall with regards

262    to the surface chemistries, the molecules observed on all the surfaces were those likely to be

263    related to the cutin structure of the surface.[14] The results demonstrate that the main differences

264    in the surface chemistry were related to the disordered arrangement of wax-like chains (*Prunus*

265    *laurocerasus* and *Hosta sieboldiama*), in addition to the C=O and $\nu_{\alpha s}$ CH$_2$ group of the *Hosta*

266    *sieboldiama*.
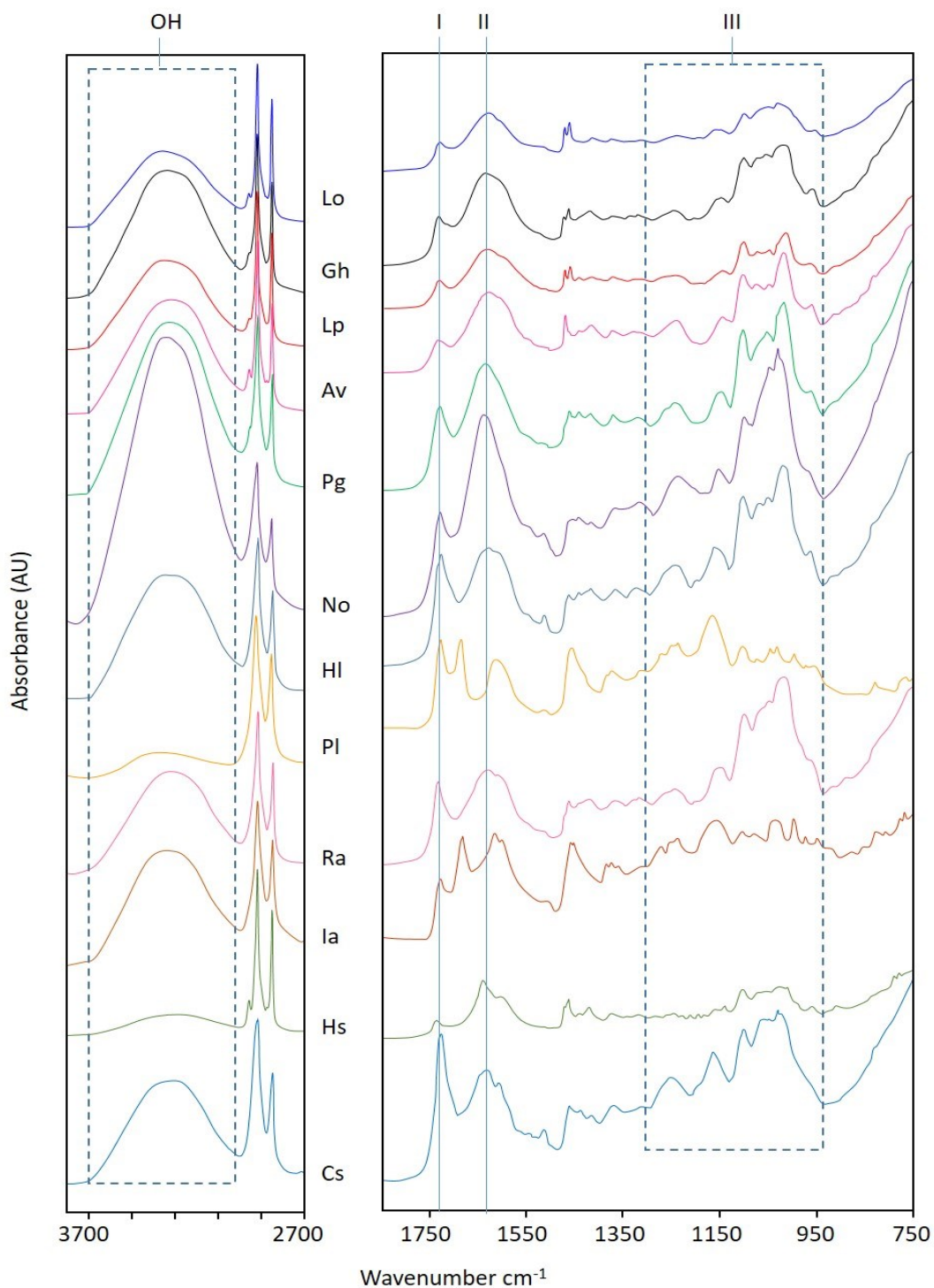
**Figure 4.** ATR-FTIR spectra showing OH and CH stretching and fingerprint regions of the leaf surfaces (leaf coding is as for Figure 3). Note that absorbance has been normalised to the C-H stretching bands to compensate for differences in effective contact area. Band I: carbonyl stretching from esters and other carbonyl compounds; Band II: assigned to the H-OH bending vibration of water; Bands III: various C-O stretching and C-N stretching vibrations.

273    Overall, there were some clear demarcations in the surface properties and composition

274    of the leaf samples. The *Lathyrus odoratus*, *Gladiolus hybridus,* and *Lupinus polyphyllus* were

275    the most hydrophobic with $\Delta G_{iwi}$ values of -91.7, -91.3, and -74.7 mJ/m$^2$, respectively. Their

276    surface properties fitted with the Cassie-Baxter model of self-cleaning surfaces and they shared

277    common traits such as high $S_a$, $S_q$, and $S_{pv}$ values, and low $\gamma_s^{LW}$, $\gamma_s^{AB}$, and $\gamma_s^-$ components.

278    However, the surface topography of the *Lathyrus odoratus* and *Lupinus polyphyllus* was

279    characterised by platelet-like features, whereas the *Gladiolus hybridus* surface was populated

280    by a homogenous distribution of raised nodules. The presence of wax nanocrystals was also

281    evident on all three surfaces. Furthermore, their ATR-FTIR spectra exhibited splitting of the $\nu_s$

282    CH$_2$ and $\nu$ CH$_2$ bands. This indicated hydrocarbon wax crystallisation, which was in agreement

283    with the SEM images that showed distinct wax crystallisation on their surfaces. Thus, it

284    appeared that a high degree of surface roughness and the presence of a dense population of wax

285    nanocrystals corresponded to a very hydrophobic leaf surface. However, it did not appear that

286    the shape of the surface features distinctly influenced its hydrophobicity. This fits with the

287    Cassie-Baxter model, whereby air (or gas) pockets may be trapped in the cavities of a rough

288    surface, resulting in a hydrophobic surface due to a composite interface with air pockets trapped

289    under the droplet.[30] It has also been suggested that nanoroughness is required to support

290    nanodroplets.[31,32] Thus, it might be likely that an interplay of all these factors resulted in the

291    most hydrophobic surfaces, although the exact parameters that impact this effect are still

292    unclear.

293    The *Aquilegia vulgaris* was the fourth most hydrophobic surface and had greater $\gamma_s^{AB}$

294    and $\gamma_s^-$ components, as well as less splitting of the $\nu_s$ CH$_2$ and $\nu$ CH$_2$ bands compared with the

295    three most hydrophobic leaves. The *Pelargonium graveolens* was the fifth most hydrophobic

296    surface and the only one with distinct trichomes. The *Pelargonium graveolens* had higher $\gamma_s^{LW}$,

297    $\gamma_s^{AB}$, and $\gamma_s^+$ components than the four most hydrophobic surfaces which is likely influenced by

298    the trichomes on its surface. Godeau et al.[33] observed that the trichomes on *Echeveria pulvinata*

299    leaves were hydrophobic, whilst the surface from which the trichomes protruded was

300    hydrophilic. Water droplets may also rest on the trichomes as perfect spheres which means they

301    can easily run off the leaves.[1]

302         The surfaces with intermediate hydrophobicity (*Nymphaea odorata*, *Hyacinthus*

303    *litwinovii*, *Prunus laurocerasus*, and *Rhododendron azaleastrum*) had mostly featureless

304    topographies, with the exception of the *Hyacinthus litwinovii* (platelet-like features).

305    Furthermore, there were no clear trends in their surface roughness or physicochemical values.

306    From the analysis, it was expected that the *Nymphaea odorata* would have been more

307    hydrophobic. However, the *Nymphaea odorata* surfaces used in this work had very few

308    topographical features. Additionally, compared to the other leaves, the *Nymphaea odorata*

309    surface exhibited intense OH stretching bands in the ATR-FTIR results, which would render

310    the surface more polar, and hence less hydrophobic. This effect may have been due to the age

311    of the leaf,[2,34] thus suggesting that further studies are required to determine the surfaces of

312    leaves over time with respect to changes in their self-cleaning and water repellent properties.

313

314    *PCA and PLSR modelling of surface chemistry data*

315         The ATR-FTIR spectral data provided a basis for further statistical analysis of the

316    leaves. PCA was performed to analyse the results of the ATR-FTIR measurements to provide

317    a greater understanding of the relationships between the variables within the data.[29] The PCA

318    data is presented using score plots labelled by leaf type on the top and class (i.e. level of

319    hydrophobicity) on the bottom (Figure 5), in addition to the loading plots of the first three

320    principal components (Figure 6). Analysing the loading plots (Figure 6) for each of the

321    principal components enabled the determination of which section(s)/peaks of the ATR-FTIR

322    spectra were influential in the relative positioning of the leaves in PCA and could be used to

323  relate back to the original spectra. Additionally, analysing the PCA when categorising the

324  samples according to their classification (surface wettability) revealed that the most

325  hydrophobic leaves shared common surface chemistry traits, demonstrated by being grouped

326  in close proximity with low intra-class variability (Figure 5, bottom). Based on their placement

327  in principal component 1 (PC1), it was concluded that the most hydrophobic leaves had strong

328  peaks pertaining to the OH stretching band, which could be observed when analysing the raw

329  data (Figure 5, bottom). The hydrophobic leaves also exhibited strong asymmetric ($\nu_{as}$ $CH_2$)

330  and symmetric ($\nu_s$ $CH_2$) methylene C-H stretching peaks at ~2916 and ~2846 $cm^{-1}$,

331  respectively, in addition to weak carbonyl ester peaks at ~1735 $cm^{-1}$. Furthermore, one of the

332  peaks that was a unique contributor to principal component 3 (PC3) included the split $CH_2$ peak

333  (~1475 $cm^{-1}$) methylene asymmetric ($\nu_{as}$ $CH_2$) C-H deformation which was only present in the

334  most hydrophobic leaves. This peak is indicative of non-cutin wax structures. In contrast, the

335  least hydrophobic leaves have highly-variable surface chemistry as measured by ATR-FTIR,

336  demonstrated by their scattered positions in the score plots. Interestingly, with the exception of

337  a few of the leaf samples, the hydrophobic and less-hydrophobic classified leaves could almost

338  be completely separated on the basis of their position according to PC3. This indicated that the

339  characteristics that contributed to this principal component could be used to distinguish

340  between these classifications and that their profile/values for these bands and corresponding

341  functional groups were very important in determining the hydrophobicity of a surface.
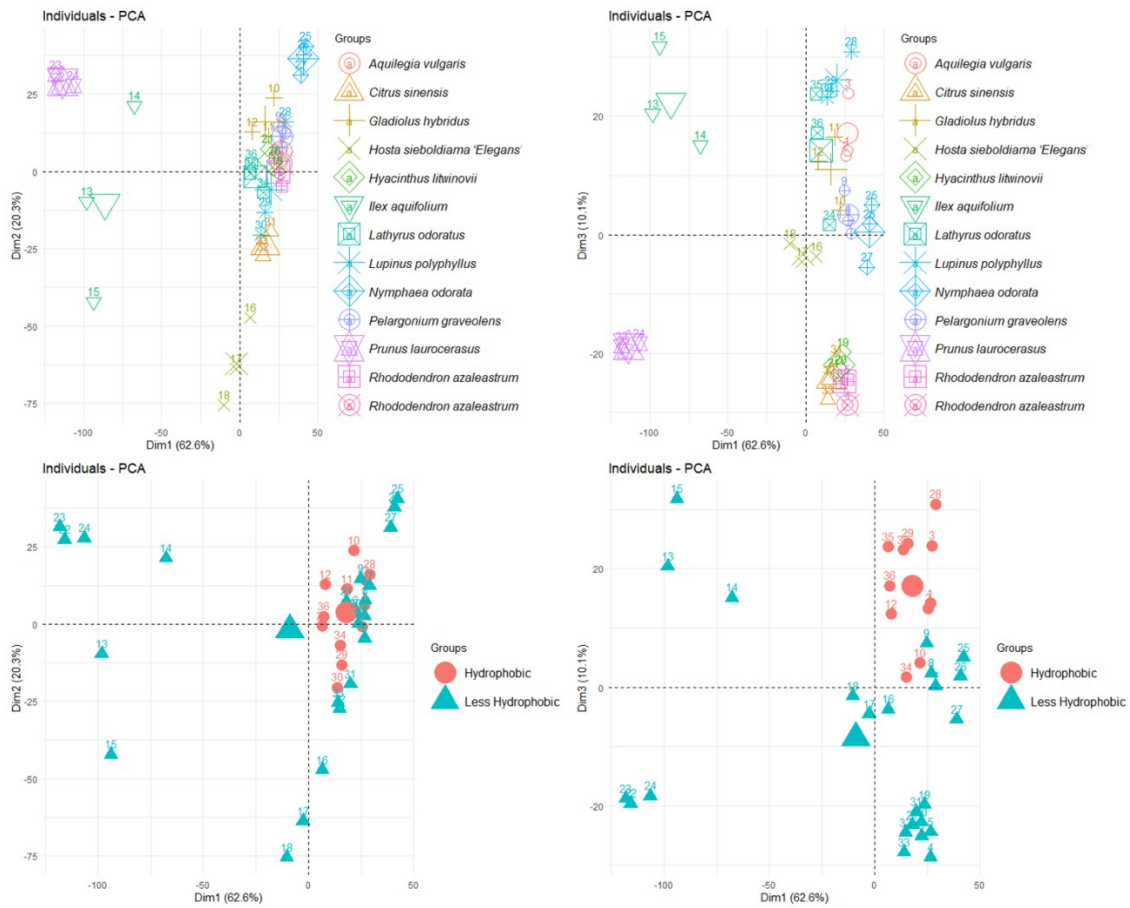
**Figure 5.** Score plots labelled by leaf type (top) and class, i.e. hydrophobicity, (bottom) of PC1 vs PC2 (left) and PC1 vs PC3 (right) for the PCA of the ATR-FTIR spectra.
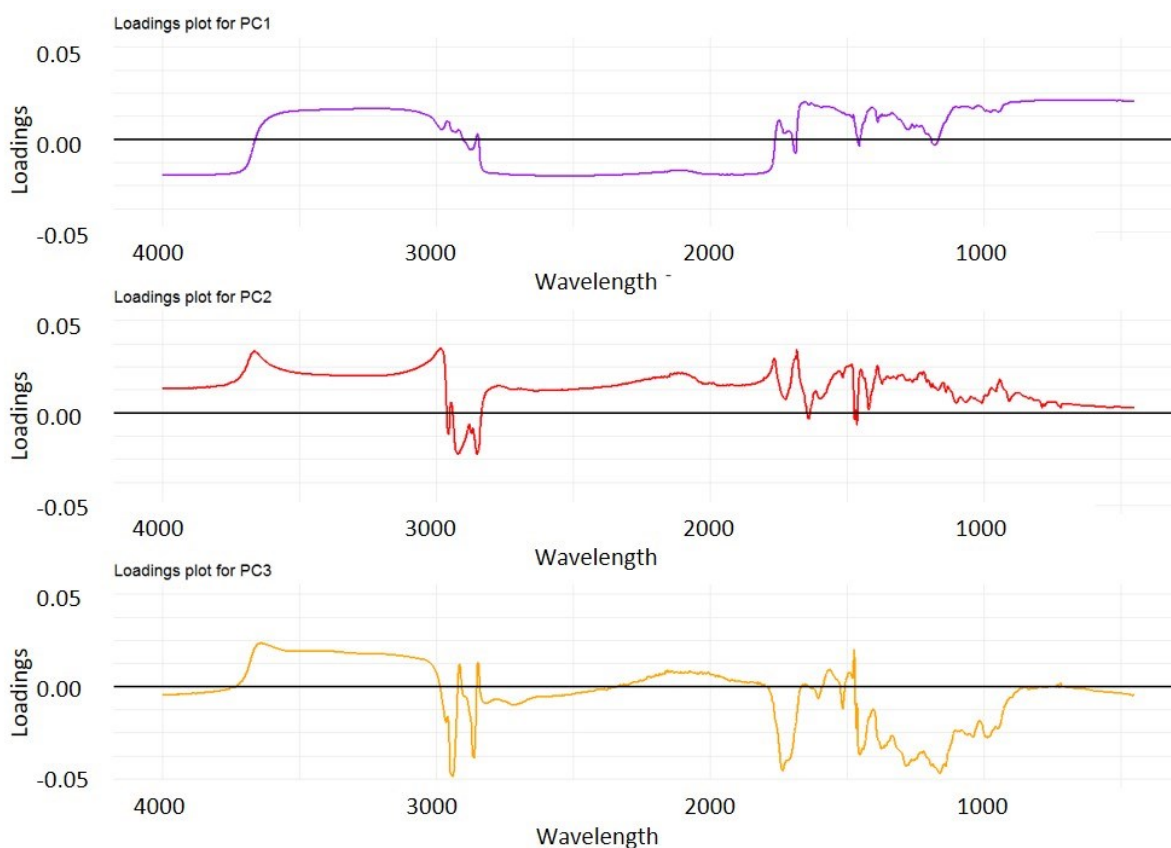
**Figure 6.** Loading plots for the PCA of the ATR-FTIR spectra of the first three PCs. PC1 (top), PC2 (middle), and PC3 (bottom).

Assessing the data by leaf type, it was clear that the ATR-FTIR of *Prunus laurocerasus* and *Ilex aquifolium* were very distinct from each other, as well as the other leaves in terms of the components that contribute to PC1 (Figure 5, top). Additionally, the *Hosta sieboldiama* was different from the other leaves ($v_{as}$ $CH_2$, C=O) that contributed to PC2. On the determination of which areas of the ATR-FTIR spectra had distinct loadings for PC2 compared to the other PCs, it was observed that PC2 featured (among others) peaks at 2925 and 1640 cm$^{-1}$ (downwards), and was the only PC that had notable influence by peaks in the 800-650 cm$^{-1}$ range (Figure 6 middle). In contrast to the other leaf samples, *Hosta sieboldiama* exhibited a notable peak centred at ~2925 cm$^{-1}$ shouldering the $v_s$ $CH_2$ band (ca. 2916 cm$^{-1}$) and was the only leaf to exhibit a sharp absorption at 1640 cm$^{-1}$. Furthermore, the *Hosta sieboldiama* leaves

359    showed a very strong peak in the C-H rocking ($\nu$ CH$_2$) region at ~720 cm$^{-1}$, an area that also

360    influences PC2 and further accounts for its marked positioning in PC2 away from other leaves.

361        While differences in various methylene frequencies were largely demonstrated by PC2,

362    the broad hydrogen bonded OH stretching band centred at 3300 cm$^{-1}$ was a main contributor to

363    PC1 (Figure 6, top). As such, the positioning of the species along the horizontal axes of all the

364    score plots in Figure 5, representing PC1, was demonstrative of the strength of this peak. As

365    aforementioned, this peak was very weak for *Prunus laurocerasus* which explains its leftmost

366    position in the PCA score plots. Furthermore, this peak was also weak for the *Ilex aquifolium*

367    and *Hosta sieboldiama*, and thus they were also positioned on the left side in PC1. In contrast,

368    the *Nymphaea odorata* had the most prominent OH stretching band, accounting for its

369    rightmost positioning in PC1. The H-O bending modes at ca. 1630 cm$^{-1}$ also contributed to

370    PC1, with lower intensity peaks differentiating *Prunus laurocerasus* and *Ilex aquifolium* from

371    the other samples. It can be surmised that PC1 was mostly influenced by ATR-FTIR peaks

372    attributable to O-H bands (stretching ~3300 and 1630 cm$^{-1}$), while PC2 was most influenced

373    by C-H methylene-related bands.

374        In addition to the PCA, further statistical analysis was performed using PLSR to model

375    the leaves WCA, and hence their surface wettability from the ATR-FTIR measurements. To

376    the Authors knowledge, this was the first time that such a model has been implemented on a

377    complex biological system, whereby an attempt using such a system was used to determine if

378    it was possible to relate surface chemistry and WCA. It was found that the PLSR model was

379    able to account for ~95% of the variation in WCA with eight components. This showed that

380    extremely variable data was able to be explained by the developed model, indicating a high

381    level of applicability of such a system to analyse complex data. Analysing the loading plot

382    (Figure S1) for the first three principal components for the model (PC1, 85%, black solid line;

383    PC2, 8%, red dashed line and PC3, 5%, green dotted line), observations could be made about

384    the influence of various bands in the ATR-FTIR spectra that were most influential to this

385    model, in relation to the WCA of the leaf surface. As seen following PCA, PC1 for this model

386    was strongly influenced by the prominent OH stretching band centred at 3300 cm$^{-1}$, whilst PC2

387    was largely influenced by this peak but also the asymmetric and symmetric methylene $CH_2$ C-

388    H stretching peaks at ~2916 cm$^{-1}$ and ~2846 cm$^{-1}$, respectively. These bands within the loading

389    plots were the main contributors to these principal components which attests to their

390    importance and influence on the WCAs. Validation of the resulting regression model from this

391    analysis indicated very good correlation ($R^2$ = 0.86) between measured and predicted values,

392    indicating its potential for predicting surface hydrophobicity from ATR-FTIR spectra of a

393    given surface (see Figure S2 for the plot depicting the performance of the PLSR model).

394        The PCA identified the *Prunus laurocerasus* and *Ilex aquifolium* surfaces as being

395    chemically different to the other leaves. Both these surfaces demonstrated disordered (liquid-

396    like) arrangements of long alkyl chains which may have contributed to their differentiation in

397    the PCA. The least hydrophobic surfaces, the *Ilex aquifolium*, *Hosta sieboldiama*, and *Citrus*

398    *sinensis*, had the lowest $\Delta G_{iwi}$ values of -6.0, -5.7, and -2.3 mJ/m$^2$, respectively. These surfaces

399    also had the highest $\gamma_s$, $\gamma_s^{AB}$, and $\gamma_s^-$ values. Differentiation in the surface topographies of the

400    three least hydrophobic leaves was more complex compared with the more hydrophobic

401    surfaces. However, the $S_a$ and $S_q$ values of the surfaces were generally lower than the other

402    plant surfaces with the exception of the *Nymphaea odorata* and *Prunus laurocerasus*. Both the

403    *Ilex aquifolium* and *Citrus sinensis* had surfaces with subtle features. Waxes may influence the

404    chemical difference in the leaves and may be detected using FTIR, even if they occur as filling

405    material within the basic cutin network (intracuticular) rather than being present on top of the

406    cuticle (epicuticular).[35]

407        The *Hosta sieboldiama* was an anomaly among the leaf samples as it exhibited distinct

408    surface features characterised by platelet-like protrusions, but was the second most wettable

409     surface. It also had a high $\gamma_s^-$ value, in addition to a higher energy shoulder on the $\nu_{as}$ CH$_2$ band

410     and a strong sharp absorption at 1640 cm$^{-1}$ that was not present in any of the other spectra. This

411     peak can be attributed to C=O carbonyl groups present, which demonstrated polar attributes.

412     These features were further highlighted in the PCA, particularly with regard to the positioning

413     within PC2. The ATR-FTIR spectrum of the *Hosta sieboldiama* exhibited a shoulder on the

414     methylene C-H stretch at ~2925 cm$^{-1}$, which indicated that different hydrocarbons were present

415     in this species. This was represented in the PCA through the distinct positioning away from the

416     other species. These hydrocarbons may be associated with polar areas that could contribute to

417     the high $\gamma_s^-$ values. Furthermore, in the H-OH bend band, the *Hosta sieboldiama* had another

418     absorption (1640 cm$^{-1}$) superimposed within the spectra, which was also accompanied by a

419     small doublet peak at 787 and 777 cm$^{-1}$. These peaks may be assignable to amine or amide

420     moieties which contributed to the high $\gamma_s^-$ values recorded. These observations are likely to be

421     related to the presence of polar domains on the *Hosta sieboldiama* leaf, which in this case, had

422     a dominant effect on surface hydrophobicity rather than the surface topography.

423        The leaf surfaces studied in this work exhibited a range of different properties and yet

424     all were water repellent and self-cleaning. An elegant explanation was offered by Zhang et al.[36]

425     as to why droplets on surfaces with features that are associated with the highly adhesive Wenzel

426     state can also be self-cleaning, like those surfaces that display the typical Lotus attributes

427     associated with the Cassie-Baxter state. It is known that on surfaces consistent with Cassie-

428     Baxter properties, self-cleaning is achieved due to low contact angle hysteresis and small

429     hydrodynamic resistance. Zhang et al.[36] further suggested that on surfaces in the Wenzel state,

430     small neighbouring droplets can coalesce into bigger ones, and the corresponding release of

431     surface energy results in a transition to the Cassie-Baxter state, and therefore self-cleaning

432     action is achieved.

Two methods of additional statistical analysis, PCA and PLSR, were used to explore and enhance the relationship between the surface chemistry characteristics, as measured using ATR-FTIR, and the surface wettability. PCA is an excellent and powerful tool to detect any underlying clusters and groupings in the data when analysing the entire surface chemistry profile. Additionally, as this technique does not make any assumptions about the data, nor does it take into account existing classifications, any notable patterns and trends found using this unsupervised approach can be confidently surmised to exist based on the ATR-FTIR spectra, not their classification. Differences seen between sample classes (i.e. hydrophobic vs less hydrophobic surfaces and different species) and the contributing factors to those differences provide insight into what distinguishes them. In our analysis, we were not only able to identify characteristics of hydrophobic leave surfaces and what are common features amongst leaves of this type, but were also able to identify species that were particularly unique and what about them was so discernible (i.e. *Prunus laurocerasus* and *Ilex aquifolium*). This analysis was based exclusively on the surface chemistry derived from ATR-FTIR spectra and clearly demonstrates the influence of surface chemistry on the wettability of leaf surfaces; the hydrophobicity of leaf surfaces is therefore not only dependent on surface topography and physicochemical properties.

Similar to PCA, the PLSR model was used to analyse the entire ATR-FTIR spectra, although this model was concerned with equating the quantitative variable, WCA, as a critical measure of surface wettability. The PLSR model found similar bands in the ATR-FTIR to be the most important at influencing surface wettability. Furthermore, the presented PLSR model showed excellent performance in validation (using a leave-one-out technique) and based on these results, it could be suggested that leaf WCA (i.e. hydrophobicity) can be predicted using ATR-FTIR surface chemistry data. As such, this finding has the potential to change the way in which surface chemistry is viewed in the design of new materials based on plant-related natural

458     surfaces. This is the first time such an analysis has shown the importance of surface chemistry

459     in a range of leaf types and our produced model can be utilised to investigate and predict the

460     water contact angle of a range of biological surfaces.

461

462     **CONCLUSIONS**

463         The physicochemical, chemical, and topographical properties of leaves obtained from

464     twelve diverse plant varieties were examined and the results demonstrated that the most

465     hydrophobic surfaces had low carbonyl species, ordered platelet-like structures, high roughness

466     values, high $\gamma_s$ and $\gamma_s^{LW}$ values, and low $\gamma_s^{AB}$ and $\gamma_s^-$ values. However, regardless of the surface

467     properties, all the leaves were self-cleaning. Using PCA, when categorising the samples

468     according to their chemical classification, it was observed that the more hydrophobic leaves

469     shared common surface chemistry traits, demonstrated by being grouped in close proximity

470     with low intra-class variability. In contrast, the less hydrophobic leaves had highly-variable

471     surface chemistry as measured by ATR-FTIR. Nevertheless, this variability in surface

472     chemistry was able to accurately model, through PLSR, leaf water contact angle with excellent

473     ability. This is the first time that the importance of surface chemistry in a range of leaf types

474     has been demonstrated. As such, these results may change the way that surface chemistry is

475     viewed in the design of new biomimetic materials based on plant surfaces. Furthermore, the

476     presented model could be used for the fast screening and determination of the water contact

477     angles of a range of biological surfaces.

478         Extensive work has been carried out on fabricating surfaces with well-defined

479     topographical features to produce hydrophobic and self-cleaning properties. However,

480     examples taken from nature clearly demonstrate that less hydrophobic, almost featureless

481     surfaces may also possess self-cleaning and non-wetting properties. A complete understanding

482     of the interactions between the magnitude and shape of surface topography, chemistry, and

483 physiochemistry, in addition to their influence on the self-cleaning action of surfaces has still

484 not been elucidated. In future work, we intend to design novel surfaces based on these

485 parameters and assess their self-cleaning properties in a range of experimental assays to

486 determine their use in specific, applied applications.

487

488 **FUNDING**

491

492 **ASSOCIATED CONTENT**

493 The Supporting Information is available free of charge at

494 Table providing surface free energy components of test liquids; Graphs predicting the

495 WCAs from the ATR-FTIR using PLSR.

496

497 **CONFLICTS OF INTEREST**

498 The authors declare no competing financial interest.

499

500 **REFERENCES**

501 (1)    Hsu, S.-H.; Woan, K.; Sigmund, W. Biologically Inspired Hairy Structures for

502        Superhydrophobicity. *Mater. Sci. Eng. R Reports* **2011**, *72*, 189–201.

503        https://doi.org/10.1016/j.mser.2011.05.001.

504 (2)    Wang, G.; Guo, Z.; Liu, W. Interfacial Effects of Superhydrophobic Plant Surfaces: A

505        Review. *J. Bionic Eng.* **2014**, *11*, 325–345. https://doi.org/10.1016/S1672-

506        6529(14)60047-0.

507    (3)    Barthlott, W.; Mail, M.; Neinhuis, C. Superhydrophobic Hierarchically Structured

508          Surfaces in Biology: Evolution, Structural Principles and Biomimetic Applications.

509          *Philos. Trans. R. Soc. A Math. Phys. Eng. Sci.* **2016**, *374*, 20160191.

510          https://doi.org/10.1098/rsta.2016.0191.

511    (4)    Barthlott, W.; Neinhuis, C. Purity of the Sacred Lotus, or Escape from Contamination

512          in Biological Surfaces. *Planta* **1997**, *202*, 1–8. https://doi.org/10.1007/s004250050096.

513    (5)    Peter, A.; Lutey, A. H. A.; Faas, S.; Romoli, L.; Onuseit, V.; Graf, T. Direct Laser

514          Interference Patterning of Stainless Steel by Ultrashort Pulses for Antibacterial

515          Surfaces. *Opt. Laser Technol.* **2020**, *123*, 105954.

516          https://doi.org/10.1016/j.optlastec.2019.105954.

517    (6)    Rajab, F. H.; Liauw, C. M.; Benson, P. S.; Li, L.; Whitehead, K. A. Production of

518          Hybrid Macro/Micro/Nano Surface Structures on Ti6Al4V Surfaces by Picosecond

519          Laser Surface Texturing and Their Antifouling Characteristics. *Colloids Surfaces B*

520          *Biointerfaces* **2017**, *160*, 688–696. https://doi.org/10.1016/j.colsurfb.2017.10.008.

521    (7)    Rajab, F. H.; Liauw, C. M.; Benson, P. S.; Li, L.; Whitehead, K. A. Picosecond Laser

522          Treatment Production of Hierarchical Structured Stainless Steel to Reduce Bacterial

523          Fouling. *Food Bioprod. Process.* **2018**, *109*, 29–40.

524          https://doi.org/10.1016/j.fbp.2018.02.009.

525    (8)    Lutey, A. H. A.; Gemini, L.; Romoli, L.; Lazzini, G.; Fuso, F.; Faucon, M.; Kling, R.

526          Towards Laser-Textured Antibacterial Surfaces. *Sci. Rep.* **2018**, *8*, 10112.

527          https://doi.org/10.1038/s41598-018-28454-2.

528    (9)    Aryal, B.; Neuner, G. Leaf Wettability Decreases along an Extreme Altitudinal

529          Gradient. *Oecologia* **2010**, *162*, 1–9. https://doi.org/10.1007/s00442-009-1437-3.
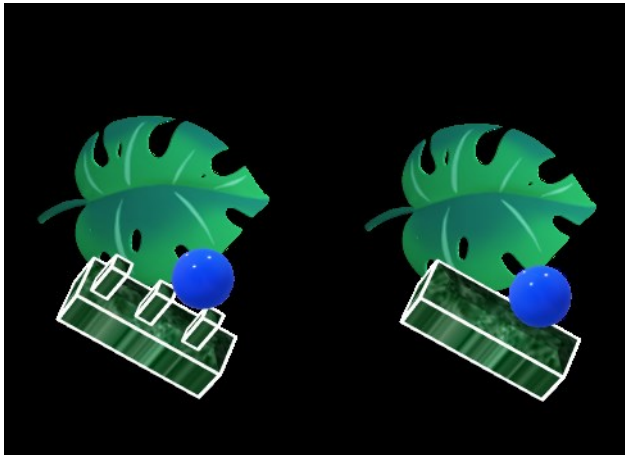
530     (10)     Ensikat, H. J.; Ditsche-Kuru, P.; Neinhuis, C.; Barthlott, W. Superhydrophobicity in

531           Perfection: The Outstanding Properties of the Lotus Leaf. *Beilstein J. Nanotechnol.*

532           **2011**, *2*, 152–161. https://doi.org/10.3762/bjnano.2.19.

533     (11)     Balsdon, J. A.; Braman, S. K.; Espelie, K. E. Biology and Ecology of Anagrus

534           Takeyanus (Hymenoptera: Mymaridae), an Egg Parasitoid of the Azalea Lace Bug

535           (Heteroptera: Tingidae). *Environ. Entomol.* **1996**, *25*, 383–389.

536           https://doi.org/10.1093/ee/25.2.383.

537     (12)     Wang, Y.; Braman, S. K.; Robacker, C. D.; Latimer, J. G.; Espelie, K. E. Composition

538           and Variability of Epicuticular Lipids of Azaleas and Their Relationship to Azalea

539           Lace Bug Resistance. *J. Am. Soc. Hortic. Sci.* **1999**, *124*, 239–244.

540           https://doi.org/10.21273/jashs.124.3.239.

541     (13)     Jetter, R.; Schäffer, S.; Riederer, M. Leaf Cuticular Waxes Are Arranged in

542           Chemically and Mechanically Distinct Layers: Evidence from Prunus Laurocerasus L.

543           *Plant, Cell Environ.* **2000**, *23*, 619–628. https://doi.org/10.1046/j.1365-

544           3040.2000.00581.x.

545     (14)     Ribeiro da Luz, B. Attenuated Total Reflectance Spectroscopy of Plant Leaves: A Tool

546           for Ecological and Botanical Studies. *New Phytol.* **2006**, *172*, 305–318.

547           https://doi.org/10.1111/j.1469-8137.2006.01823.x.

548     (15)     J. A. Hardin; C. L. Jones; P. R. Weckler; N. O. Maness; Madden, R. D. Rapid

549           Quantification of Spinach Leaf Cuticular Wax Using Fourier Transform Infrared

550           Attenuated Total Reflectance Spectroscopy. *Trans. ASABE* **2013**, *56*, 331–339.

551           https://doi.org/10.13031/2013.42579.

552     (16)     Tu, C.-W.; Tsai, C.-H.; Wang, C.-F.; Kuo, S.-W.; Chang, F.-C. Fabrication of

553           Superhydrophobic and Superoleophilic Polystyrene Surfaces by a Facile One-Step

554    Method. *Macromol. Rapid Commun.* **2007**, *28*, 2262–2266.

555    https://doi.org/10.1002/marc.200700447.

556    (17)    Wang, H.; Shi, H.; Li, Y.; Wang, Y. The Effects of Leaf Roughness, Surface Free

557    Energy and Work of Adhesion on Leaf Water Drop Adhesion. *PLoS One* **2014**, *9*,

558    e107062. https://doi.org/10.1371/journal.pone.0107062.

559    (18)    van Oss, C. J.; Good, R. J.; Chaudhury, M. K. The Role of van Der Waals Forces and

560    Hydrogen Bonds in "Hydrophobic Interactions" between Biopolymers and Low

561    Energy Surfaces. *J. Colloid Interface Sci.* **1986**, *111*, 378–390.

562    https://doi.org/10.1016/0021-9797(86)90041-X.

563    (19)    van Oss, C. J. Hydrophobicity of Biosurfaces - Origin, Quantitative Determination and

564    Interaction Energies. *Colloids Surfaces B Biointerfaces* **1995**, *5*, 91–110.

565    https://doi.org/10.1016/0927-7765(95)01217-7.

566    (20)    van Oss, C. J.; Giese, R. F. The Hydrophilicity and Hydrophobicity of Clay Minerals.

567    *Clays Clay Miner.* **1995**, *43*, 474–477. https://doi.org/10.1346/CCMN.1995.0430411.

568    (21)    Bos, R.; Busscher, H. J. Role of Acid-Base Interactions on the Adhesion of Oral

569    Streptococci and Actinomyces to Hexadecane and Chloroform - Influence of Divalent

570    Cations and Comparison between Free Energies of Partitioning and Free Energies

571    Obtained by Extended DLVO Analysis. *Colloids Surfaces B Biointerfaces* **1999**, *14*,

572    169–177. https://doi.org/10.1016/S0927-7765(99)00034-X.

573    (22)    Skovager, A.; Whitehead, K.; Wickens, D.; Verran, J.; Ingmer, H.; Arneborg, N. A

574    Comparative Study of Fine Polished Stainless Steel, TiN and TiN/Ag Surfaces:

575    Adhesion and Attachment Strength of Listeria Monocytogenes as Well as Anti-

576    Listerial Effect. *Colloids Surfaces B Biointerfaces* **2013**, *109*, 190–196.

577    https://doi.org/10.1016/j.colsurfb.2013.03.044.

578   (23)   Whitehead, K. A.; Smith, L. A.; Verran, J. The Detection and Influence of Food Soils

579           on Microorganisms on Stainless Steel Using Scanning Electron Microscopy and

580           Epifluorescence Microscopy. *Int. J. Food Microbiol.* **2010**, *141*, S125–S133.

581           https://doi.org/10.1016/j.ijfoodmicro.2010.01.012.

582   (24)   Mirabella, F. M. *Principles, Theory, and Practice of Internal Reflection Spectroscopy*;

583           2006. https://doi.org/10.1201/9781003066941-2.

584   (25)   Team, R. C. The R Project For Statistical Computing. 2015.

585   (26)   Team, R. C. A Language And Environment For Statistical Computing. 2015.

586   (27)   Wickham, H. Elegant Graphics For Data Analysis. 2016.

587   (28)   Mevik, B.-H.; Wehrens, R.; Liland, K. H. Suggests, Package 'Pls.' 2019.

588   (29)   Camacho, J.; Picó, J.; Ferrer, A. Data Understanding with PCA: Structural and

589           Variance Information Plots. *Chemom. Intell. Lab. Syst.* **2010**, *100*, 48–56.

590           https://doi.org/10.1016/j.chemolab.2009.10.005.

591   (30)   Schulte, A. J.; Droste, D. M.; Koch, K.; Barthlott, W. Hierarchically Structured

592           Superhydrophobic Flowers with Low Hysteresis of the Wild Pansy (Viola Tricolor) -

593           New Design Principles for Biomimetic Materials. *Beilstein J. Nanotechnol.* **2011**, *2*,

594           228–236. https://doi.org/10.3762/bjnano.2.27.

595   (31)   Nosonovsky, M.; Bhushan, B. Biomimetic Superhydrophobic Surfaces: Multiscale

596           Approach. *Nano Lett.* **2007**, *7*, 2633–2637. https://doi.org/10.1021/nl071023f.

597   (32)   Bhushan, B.; Jung, Y. C. Micro- and Nanoscale Characterization of Hydrophobic and

598           Hydrophilic Leaf Surfaces. *Nanotechnology* **2006**, *17*, 2758–2772.

599           https://doi.org/10.1088/0957-4484/17/11/008.

(33) Godeau, G.; Laugier, J.-P.; Orange, F.; Godeau, R.-P.; Guittard, F.; Darmanin, T. A Travel in the Echeveria Genus Wettability's World. *Appl. Surf. Sci.* **2017**, *411*, 291–302. https://doi.org/10.1016/j.apsusc.2017.03.192.

(34) BOYCE, R. L.; McCUNE, D. C.; BERLYN, G. P. A Comparison of Foliar Wettability of Red Spruce and Balsam Fir Growing at High Elevation. *New Phytol.* **1991**, *117*, 543–555. https://doi.org/10.1111/j.1469-8137.1991.tb00959.x.

(35) Barthlott, W.; Mail, M.; Bhushan, B.; Koch, K. Plant Surfaces: Structures and Functions for Biomimetic Innovations. *Nano-Micro Lett.* **2017**, *9*, 23. https://doi.org/10.1007/s40820-016-0125-1.

(36) Zhang, K.; Li, Z.; Maxey, M.; Chen, S.; Karniadakis, G. E. Self-Cleaning of Hydrophobic Rough Surfaces by Coalescence-Induced Wetting Transition. *Langmuir* **2019**, *35*, 2431–2442. https://doi.org/10.1021/acs.langmuir.8b03664.

614    TOC Graphic



615